Small-Angle X-ray Scattering Study on the Tensile Fracture Process of Poly(ethylene terephthalate) Fiber

Masatoshi Shioya,*,† Tomomi Kawazoe,† Ryota Okazaki,† Takumi Suei,† Shinichi Sakurai,‡ Katsuhiro Yamamoto,∮ and Takeshi Kikutani†

Graduate School of Science and Engineering, Department of Organic and Polymeric Materials, Tokyo Institute of Technology, S8-34, 2-12-1 O-okayama, Meguro-ku, Tokyo 152-8552, Japan, Graduate School of Science and Technology, Kyoto Institute of Technology, Matsugasaki, Sakyo-ku, Kyoto 606-8585, Japan, and Graduate School of Engineering, Nagoya Institute of Technology, Gokiso-cho, Showa-ku, Nagoya 466-8555, Japan

Received December 11, 2007; Revised Manuscript Received March 2, 2008

ABSTRACT: Time-resolved small-angle X-ray scattering measurements using synchrotron radiation have been conducted during tensile deformation of a poly(ethylene terephthalate) fiber at room temperature. The marked change of the scattering patterns from the layer-line scattering with a four-spot nature to the layer-line scattering concentrated on the meridian at small fiber strains could be interpreted as the decrease in the disorder of the long-period structures without assuming the tilted lamella stack. The microvoids formed at a large fiber strain were characterized by applying a method proposed by the present author to the equatorial streak and the relative microvoid volume fraction, size and shape of the microvoid cross sections and longitudinal size of the microvoids were determined. It was inferred that the microvoids were formed in the regions which linked long-period structures, depending on the properties of these regions and the formation of microvoids contributed to the fracture toughness of the fiber.

Introduction

High-strength fibers can be produced from both rigid chain polymers like aramid and flexible chain polymers like polyethylene by utilizing the liquid crystalline spinning and the gel spinning, respectively. On the other hand, the fibers produced from polymers with intermediate chain rigidity like poly(ethylene terephthalate) (PET) show relatively lower tensile strength at the present state of technology.[1] Various attempts have been undertaken to improve the tensile strength of PET fibers.[2] For the improvement of the mechanical properties of PET fibers, understanding of the structure changes of these fibers during tensile deformation up to fracture is of importance.

The strain-induced crystallization of PET is the structure change caused by tensile deformation leading to the development of structure. This effect arises, for example, when amorphous PET is drawn at a temperature between the glass transition and the melting temperatures and when amorphous PET is annealed after drawing.[3–11] The feature of the stress−strain (S-S) curves of amorphous PET at temperatures allowing crystallization has been correlated to the structure changes by Gorlier et al.[9] and Kawakami et al.[11]

Tensile deformation of PET also causes the structure changes leading to the destruction of structure and macroscopic fracture. The influences of the flexibility of polymer chains on the change of the long period during tensile deformation have been studied by Stribeck et al.[12] for drawn and annealed bristles of PET, another polyester and poly(ether ester) type polymers. Stockfleth et al.[13] have shown that during tensile deformation of uniaxially drawn and annealed PET films, lamellar separation occurs at a small strain and microvoids are formed near the fracture. The influences of carbon black and carbon nanotube dispersed in an amorphous PET film on the evolution of crazes during tensile deformation and the fracture toughness have been studied by Kobayashi et al.[14,15]

SAXS provides useful information on the structure changes of polymers during tensile deformation since the sizes of structure components relevant to the fracture process are in a range detectable with SAXS. The uniaxially oriented semicrystalline polymers like PET and polyamide 6 (PA 6) fibers produce various SAXS patterns such as layer-line and two-spot and four-spot scattering. The layer-line scattering is the striation parallel to the equator and intersecting the meridian away from the center of the pattern. The four-spot scattering has two intensity maxima of the intensity distribution along the layer line. In some cases, the scattering patterns are curved in an elliptic arc. The four-spot scattering has been attributed to the long-period structure having inclined interfaces between the crystalline and amorphous regions in the studies of Zheng et al.[16] and Murthy et al.[17–19] In the case of highly oriented high-density polyethylene, the inclined interfaces have been evidenced with transmission electron microscopy by Song et al.[20] The scattering patterns curved in an elliptic arc have been analyzed by Murthy et al.[17,18,21] using elliptical cylindrical coordinates based on the assumption that the entire structure has an elliptic anisotropy. The present authors[22] have theoretically shown that the bundle of long-period structures produce, depending on the disorder of structure, various scattering patterns including the layer-line scattering with a four-spot nature and the scattering with a curvature without assuming inclined interfaces.

The microvoids which are originally contained or formed during tensile deformation of fibers produce an equatorial streak in the SAXS pattern. The sizes of microvoids and microfibrils formed by stretch-hold deformation of poly(vinylidene fluoride) (PVDF) fibers have been analyzed utilizing the Guinier and the Porod plots by Wu et al.[23] The sizes of the scattering objects causing equatorial streaks of poly(*p*-phenylene terephthalamide) (Kevlar) fibers have been analyzed utilizing the Porod plot by Grubb et al.[24] The present author[25,26] has characterized the microvoids in carbon fibers by proposing an analysis method with which several size parameters were determined from the equatorial streak and the size distribution, shape and electron density variation in the microvoids were determined by comparing these parameters.

---

* To whom correspondence should be addressed. Telephone and fax: +81-3-5734-2434. E-mail: shioya.m.aa@m.titech.ac.jp.

† Tokyo Institute of Technology.

‡ Kyoto Institute of Technology.

∮ Nagoya Institute of Technology.

10.1021/ma7027616 CCC: $40.75

In the present study, the time-resolved SAXS measurements have been conducted using a synchrotron radiation during tensile deformation up to fracture of a PET fiber at room temperature. The structure changes of the PET fiber during this process have been analyzed by utilizing the methods proposed by the present authors.

Experimental Section

Material. A melt spun and drawn PET fiber with a diameter of about 129 μm was used for the measurements. The PET before spinning had a melting temperature at 255 °C, a glass transition temperature at 73 °C, an intrinsic viscosity of 1.00 g dL^{-1}, and a density of 1.41 g cm^{-3}. The melt spinning was carried out at the Japan Chemical Innovation Institute using a single orifice and a spin line of 1.5 m cooled by ambient air, at a throughput rate of 1.56 g min^{-1} and a take-up velocity of 30.8 m min^{-1}. The drawing of the fiber was carried out in the following three steps: First, the fiber was drawn in water at 65 °C by a ratio of 4.0. Second, the fiber was drawn in an air-circulating oven at 150 °C by a ratio of 1.4 to a total draw ratio (TDR) of 5.6. Finally, the fiber was drawn in an air-circulating oven at 200 °C by a ratio of 1.1 to a TDR of 6.2.

WAXD Measurements. Wide-angle X-ray diffraction (WAXD) of a fiber bundle with a rectangular cross section was measured without applying deformation at room temperature using Ni-filtered Cu Kα radiation and a diffractometer. The diffraction profile as a function of the diffraction angle was measured using a position-sensitive proportional counter with the symmetrical transmission geometry at the center of the detection range. The diffraction profile as a function of the azimuthal angle was measured using a proportional counter by rotating the specimen around the bisector of the angle between the incident and the detected X-ray beams by keeping the symmetrical transmission geometry. The measured intensity distributions were corrected for the air scattering, the X-ray absorption, and the variation of the thickness between different specimens.

SAXS Measurements during Tensile Deformation. SAXS was measured during tensile deformation of the fiber at room temperature. The synchrotron radiation (BL15A, Photon Factory, High Energy Accelerator Research Organization, Japan) was used for the X-ray source. The X-ray wavelength was 0.15 nm and the cross section sizes of the incident X-ray beam were about 0.3 mm in the fiber axis direction and 0.2 mm perpendicularly to it. The X-ray beam impinged upon the fiber perpendicularly to the fiber axis. The SAXS patterns were obtained using a CCD camera with an image intensifier. A vacuum chamber was placed between the specimen and the detector separated by about 2.1 m. The scattering angle was calibrated using the SAXS peaks of collagen.

Tensile deformation was applied to the fiber using a miniature tensile testing machine (Handy tensile testing machine, AK-01, Kato Tech Co. Ltd.) mounted on a movable stage for position adjustment. The single fiber was gripped with the chucks of the tensile testing machine at a gage length of 10 mm. The position of the fiber was adjusted so that the X-ray beam impinged on the center of the fiber between the chucks. Since the chucks moved in the counter directions at the same velocity, the X-ray beam was kept incident on the same portion of the fiber during tensile deformation. The fiber was deformed at a constant velocity of 20 μm s^{-1}, i.e., 12% min^{-1}. The single PET fibers supplied for the measurements will be distinguished as samples A−K.

Results

Stress−Strain Curve and WAXD. Figure 1 shows the S–S curves of the as spun fibers (TDR = 1.0), the fiber after the first drawing stage (TDR = 4.0), the fiber after the second drawing stage (TDR = 5.6), and the finally obtained fiber (TDR = 6.2). The as spun fiber shows a clear yield point at which neck deformation commences and very large fiber strain at fracture. The S−S curves of the finally obtained fibers, samples A and B in this figure, were measured during SAXS measurements. Although these samples were prepared under the same conditions, sample B showed a larger fiber strain at fracture than sample A.

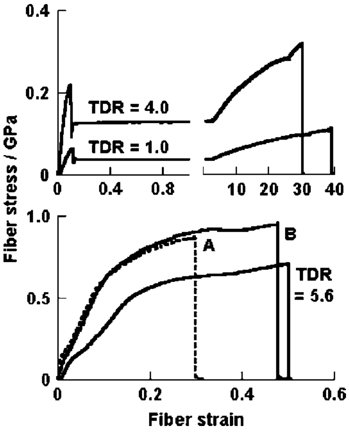

Figure 1. S−S curves of as spun fiber (TDR = 1.0), fiber after the first drawing stage (TDR = 4.0), fiber after the second drawing stage (TDR = 5.6), and the finally obtained fiber (TDR = 6.2), samples A and B.

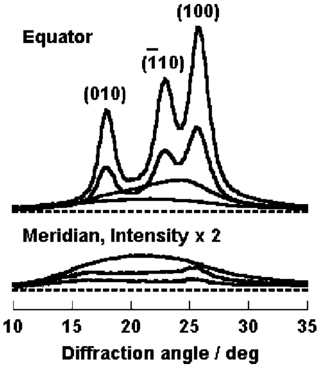

Figure 2. Equatorial and meridional WAXD profiles of as spun fiber (TDR = 1.0), fiber after the first drawing stage (TDR = 4.0), fiber after the second drawing stage (TDR = 5.6), and the finally obtained fiber (TDR = 6.2). Broken lines indicate zero intensity labels. With increasing TDR, the equatorial diffraction increased while the meridional diffraction decreased. Meridional profiles for TDR = 5.6 and 6.2 almost coincided.

The WAXD profiles of the fibers at various stages of processing are compared in Figure 2. The as spun fibers show only the amorphous halo. The finally obtained fiber produces the 010, −110, and 100 diffraction peaks as shown in the figure and the −105 diffraction peak at a diffraction angle of about 43°. The crystallite sizes of the finally obtained fiber determined using the Scherrer equation from the widths of the 100, 010, and −105 diffraction peaks are 4.3, 5.5, and 4.2 nm, respectively.

PET forms a triclinic crystallite and the lattice constants reported by Fakirov et al.[27] are $a = 0.448$ nm, $b = 0.585$ nm, $c = 1.075$ nm, $\alpha = 99.5°$, $\beta = 118.4°$, and $\gamma = 111.2°$. With this unit cell, the (−105) plane normal is inclined from the *c*-axis by 10.83°. With respect to the inclination of the *c*-axis against the machine direction, Goschel et al.[28] have reported that the *c*-axis is nearly parallel to the drawing direction for highly drawn PET films, while Daubeny et al.[29] have reported that the *c*-axes are slightly (for example, 5°) tilted from the fiber axis for most drawn PET fibers. The tilts of the (−105) plane normal and the *c*-axis from the fiber axis cause the deviations of the −105 diffraction peak from the meridian and the 100 and the 010 diffraction peaks from the equator. Ignoring these small inclinations and the broadening of diffraction peaks due to the disorder of the structure, the crystallite sizes determined from the equatorial 100, the equatorial 010, and the meridional −105 diffraction peaks can be regarded as the crystallite sizes in the *a*, *b*, and *c* axis directions, respectively.

The molecular orientation of the amorphous regions in the finally obtained fiber was very roughly estimated from WAXD as follows: It was assumed that the background intensity is independent of the azimuthal angle and varies linearly with the diffraction angle between 12 and 36°. It was also assumed that the observed intensity consists of only the amorphous diffraction and the background intensity at the diffraction angle of the minimum between the 010 and the −110 diffraction peaks and that the observed intensity consists of only the background intensity at the diffraction angles of 12 and 36°. Then the azimuthal intensity distribution of the amorphous regions can be obtained from the azimuthal intensity distribution observed at the diffraction angle of the minimum between the 010 and the −110 diffraction peaks by subtracting the background intensity determined from the straight line drawn on the equatorial profile. In the azimuthal intensity distribution of amorphous regions thus obtained, the major diffractions concentrated within an azimuthal angle range of 20° on both sides of the equator. By assuming that these diffractions are produced by the positional correlation, perpendicular to the molecular axis, between amorphous molecules, the Herman orientation function f_a which represents the distribution of the angle ϕ between the molecular axis and the fiber axis is calculated from the azimuthal intensity $I(\phi)$ as follows.

$$f_{\mathrm{a}} = \frac{3}{2}\langle\cos^2\phi\rangle - \frac{1}{2} = \frac{3\int_{-\pi/2}^{\pi/2} I(\phi)\cos^3\phi\,\mathrm{d}\phi}{2\int_{-\pi/2}^{\pi/2} I(\phi)\cos\phi\,\mathrm{d}\phi} - \frac{1}{2} \qquad (1)$$

In this equation, $\langle\ \rangle$ stands for averaging and the orientation angle ϕ equals the azimuthal angle measured from the equator. The value of f_{a} for the finally obtained fibers was estimated to be 0.88. The orientation dependent density ρ_{a} of amorphous regions was calculated with the following equation[30] as 1.344 g cm^{-3}.

$$\rho_{\mathrm{a}}/(\mathrm{g\ cm^{-3}}) = 0.0094 f_{\mathrm{a}} + 1.336 \qquad (2)$$

If the tails of the 010 and the −110 diffraction peaks of the crystalline regions with a higher orientation are involved in $I(\phi)$, the true amorphous density may be between the value shown above, and the value for the isotropic amorphous region 1.336 g cm^{-3}.

The volume fraction of the crystalline regions in the finally obtained fiber was estimated as 0.27 from the densities of the fiber, 1.390 g cm^{-3}, the crystalline regions,[27] 1.515 g cm^{-3}, and the amorphous regions, 1.344 g cm^{-3}, by assuming a two-phase model and the rule of mixture. The crystallite volume fraction was estimated as 0.30 by using 1.336 g cm^{-3} for the density of amorphous regions.

SAXS. The SAXS pattern of the PET fiber changed during tensile deformation at room temperature as shown in Figure 3. These patterns were obtained using parallel aligned 6 fibers in some other experimental facility in order to gain the scattering intensity. Except for these patterns, the results shown in this paper were obtained using single fibers as described in the Experimental Section.

The scattering patterns changed in the following manner: The PET fiber initially showed layer-line scattering with a four-spot nature. The four-spot nature suddenly disappeared by the application of a small fiber strain and the intensity distribution along the layer line concentrated on the meridian with increasing fiber strain. The separation between the two layer lines of each pattern decreased with increasing fiber strain. A strong equatorial streak appeared at a large fiber strain and increased its intensity up to fracture with increasing fiber strain. In the following, the structure changes of the PET fiber will be analyzed based on the changes in the scattering patterns.

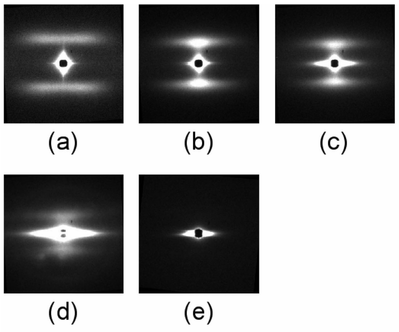

Figure 3. SAXS patterns of a bundle of 6 PET fibers under tensile deformation at room temperature. Fiber axis is in the top and bottom direction. Fiber strain increased from part a to part e where parts a and e were obtained before deformation and after fracture, respectively. Brightness was varied between patterns in order to make features clearly discernible.

Disorder of Structure. Meridional SAXS peaks of polymeric fibers are usually caused by the periodic electron density distribution in the long-period structure. A pair of crystalline and amorphous regions composes a unit cell and the unit cells are aligned in parallel to the fiber axis forming the long-period structure. Since the sizes of the reciprocal space image are inversely related to the sizes of the real space image, the long-period structure with small transverse sizes produces an array, along the meridian, of the scattering peaks which are extended in parallel to the equator. A streak on the equator is simultaneously produced by this structure, whereas it is absent from the scattering patterns of the PET fiber at small fiber strains (Figure 3).

The present authors[22] have interpreted the layer-line scattering without the equatorial streak based on a structure model which consisted of the bundle of long-period structures. The scattering pattern of the bundle of long-period structures varies depending on the disorder of the structure as follows:

(1) If the long-period structures are regularly arranged in a bundle so that the unit cells build up a regular three-dimensional lattice, the reciprocal space image of the bundle forms a three-dimensional lattice. This structure produces a spotlike scattering pattern.

(2) If the arrangements of the long-period structures are notably disordered in both transverse and longitudinal directions, the reciprocal space image of the bundle is identical, except for the intensity, with that of an isolated long-period structure, and consists of the disks with flat surfaces perpendicular to the meridian and centers aligned along the meridian. This structure gives the layer-line scattering with the equatorial streak.

(3) If the positions, in the transverse cross section of the bundle, of the long-period structures are regular while the arrangements of the transversely neighboring unit cells are notably disordered in the longitudinal direction, the bundle gives the reciprocal image which is different from point 2 in that the disk on the equatorial plane is replaced by two-dimensional lattice points. If the long-period structures are closely packed in the bundle as well, the lattice points on the equatorial plane, except for the central point, have vary low intensity. This structure gives the layer-line scattering without the equatorial streak.

(4) By adjusting the values of structure parameters, this model reproduces various scattering patterns of polymeric fibers such as the layer-line, four-spot, droplet-shaped, and triangular-shaped scattering patterns. Some of the scattering peaks of these patterns are not of ordinary integer order but are, so to speak, of the 0.5th order.[22]

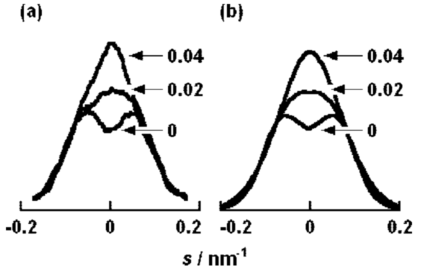

Figure 4. Measured (a) and calculated (b) intensity distributions, along the layer line, of layer-line scattering for sample B. Abscissa *s* is the equatorial component of scattering vector.

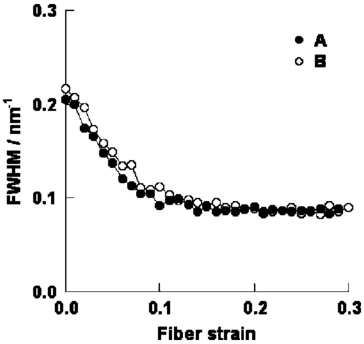

Figure 5. Fwhm of intensity distribution, along the layer line, of layer-line scattering for samples A and B versus fiber strain.

The intensity distributions, along the layer line, of the layer-line scattering of the PET fiber at small fiber strains are shown in Figure 4a. The full-widths at half-maximum (fwhm) of the intensity distributions as shown in Figure 4a are plotted against the fiber strains in Figure 5 for two samples. The four-spot nature suddenly disappears by the application of a small fiber strain (Figure 4a) and the scattering concentrates on the meridian with increasing fiber strain up to 0.1 (Figure 5). The intensity distributions similar to Figure 4(a) have already been reported by Murthy et al. for PET fibers[19] and PA 6 fibers.[18]

In the previous paper,[22] the values of structure parameters of the same PET fiber as used in the present study were determined by trial and error through the comparison of calculated and measured intensity distributions. In the calculation, it was assumed that the arrangements of the crystalline regions in the bundle had a disorder of the second kind. The vectors joining the longitudinally neighboring crystalline regions were assumed to distribute, in the longitudinal direction, in the range of $\omega_{33}|u_3|$ where $|u_3|$ is the long period. The vectors joining the transversely neighboring crystalline regions were assumed to distribute, in the longitudinal direction, in the range of $\omega_{13}|u_3|$. The structure of the PET fiber thus determined was as follows: nine long-period structures were closely packed in a bundle; each long-period structure contained four crystalline regions with the crystallite volume fraction of 0.3; the longitudinal disorder of the arrangements of the longitudinally neighboring crystalline regions ω_{33} was 0.4. Before tensile deformation, the long period $|u_3|$ was 13.8 nm and the diameter of each long-period structure was 6.2 nm. The values shown above are acceptable in comparison with the crystallite sizes and fraction. The longitudinal disorder of the arrangements of the transversely neighboring crystalline regions ω_{13} decreased with the fiber strain as shown in Figure 6. The intensity distributions calculated using these values of structure parameters well represent the measured ones as shown in Figure 4b. Figure 6 indicates that the marked changes of the scattering pattern at small fiber strains are brought about by the slight decrease in the longitudinal disorder of the arrangements of the transversely neighboring crystalline regions.

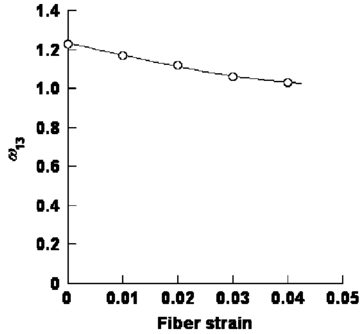

Figure 6. Longitudinal disorder of arrangements of transversely neighboring crystalline regions ω_{13} versus fiber strain for sample B.

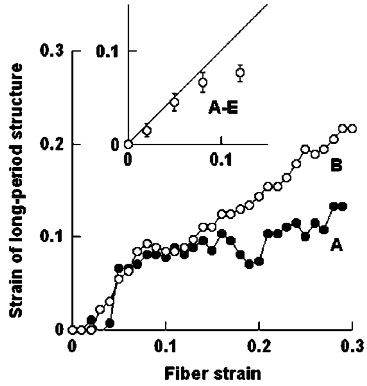

Figure 7. Strain of long-period structure for samples A and B and average strain of long-period structure for samples A–E (inset) versus fiber strain. Error bars represent standard deviations and straight line shows strain of long-period structure equal to fiber strain (inset).

Strain of Long-Period Structure. The separation between the two layer lines of each pattern decreased with increasing fiber strain. This corresponds to the increase in the length of the long-period structure. The strain of the long-period structure was calculated by applying the Bragg equation to the scattering peak of the intensity distribution, on the meridian, of the layer-line scattering. The results obtained for samples A and B are plotted against the fiber strains in Figure 7. Similar relations have already been reported by Murthy et al.[19] for PET fibers, Murthy et al.,[18] and Samon et al.[31] for PA 6 fibers and Wu et al. for PVDF fibers.[23]

At small fiber strains, the strain of the long-period structure is almost equal to the macroscopic fiber strain for both samples. For verifying the reproducibility of this result, the strain of the long-period structure was measured for five samples (samples A−E) and the average and the standard deviation are shown against the fiber strain in the inset of Figure 7. The straight line in the inset shows the strain of the long-period structure equal to the fiber strain. In this fiber strain region, the fiber stress increases linearly with the fiber strain, and the S−S curves of samples A and B almost coincide.

At the fiber strains beyond 0.1, the strain of the long-period structure is smaller than the fiber strain. The response of the long-period structure to the fiber strain for sample A is less sensitive than that for sample B. In this fiber strain region, the fibers show slower increase of the fiber stress revealing the bending of the S−S curves. The strain of the long-period structure beyond the fiber strain of about 0.3 could not be determined accurately since the meridional tail of the strong equatorial scattering overlapped on the layer-line scattering.

Microvoids. The sample with a larger fiber strain at fracture produced a strong equatorial streak when the fiber strain reached about 0.3. Simultaneously, whitening of the fiber was seen with the naked eye. Beyond this fiber strain, the fiber was deformed without showing a large increase of the fiber stress.

It is considered that the equatorial streak is produced by microvoids formed during tensile deformation. This interpretation comes from the result that the equatorial streak shows extremely stronger intensity than the layer-line scattering. The SAXS intensity is in proportion to the square of the electron density difference between structure components. The electron density difference between microvoids and surrounding solid is much larger than that between the crystalline and the amorphous regions of the long-period structure. Thus, the scattering from microvoids is much stronger than the layer-line scattering. A large aspect ratio of the equatorial streak suggests that the microvoids are extended in parallel to the fiber axis. Although the total reflection at the fiber surface also produced the equatorial streak, the scattering from the microvoids was much stronger than the total reflection.

The microvoids were characterized using a method previously reported.[25,26] The definitions of the parameters which can be determined with this method are listed below where the cross section stands for the microvoid cross section perpendicular to the fiber axis.

v: volume fraction of microvoids.

S_3: cross-section area which is averaged after weighting with the cross section area.

R_3^2: squared radius of gyration of the cross section, which is averaged after weighting with the squared cross-section area.

l_2: length of the line between two points on the contour of the cross section, which is averaged after weighting with the length of this line.

l_3: length of the line between two points on the contour of the cross section, which is number-averaged.

These definitions are somewhat complicated but they can be determined from the scattering intensity distribution without making any assumption on the shape and size of the microvoid cross sections. If it is assumed that the microvoid cross sections perpendicular to the fiber axis are of elliptic shapes with the major and the minor axes $2\mu r$ and $2r$, respectively, and μ and r distribute arbitrarily, the size parameters are represented as follows.

$$R_3^{\,2} = \frac{1}{4}\frac{\langle \mu^2(\mu^2+1)r^6\rangle}{\langle \mu^2 r^4\rangle} \tag{3}$$

$$S_3 = \pi\frac{\langle \mu^2 r^4\rangle}{\langle \mu r^2\rangle} \tag{4}$$

$$l_2 = \frac{32}{3\pi^2}\frac{\langle \mu F(\sqrt{1-\mu^{-2}})r^3\rangle}{\langle \mu r^2\rangle} \tag{5}$$

$$l_3 = \frac{\pi^2}{4}\frac{\langle \mu r^2\rangle}{\langle \mu E(\sqrt{1-\mu^{-2}})r\rangle} \tag{6}$$

In these equations, $\langle\ \rangle$ stands for the number-averaging over all the microvoid cross sections and $F(x)$ and $E(x)$ are the complete elliptic integrals of the first and the second kinds, respectively. Assuming further that the microvoid cross sections are uniform in shape and size and using approximations of $F(x)$ and $E(x)$, the size parameters are represented as follows.

$$R_3 = \frac{1}{2}\sqrt{\mu^2+1}\,r \tag{7}$$

$$S_3 = \pi\mu r^2 \tag{8}$$

$$l_2 \approx [1.698 + 0.6356(\mu-1)^{0.6196}]r \tag{9}$$

$$l_3 \approx [1.571 + 0.4659(\mu-1)^{0.3234}]r \tag{10}$$

Among these size parameters, l_3 is influenced by the electron density variation in the microvoids as well as their sizes. The electron density variation in the microvoids of carbon fibers has been estimated in a previous paper.[26]

The values of the parameters shown above can be determined from the scattering intensity distribution as follows: It is assumed that the orientation distribution of the microvoids is cylindrically symmetric and that the X-ray beam with small cross section sizes impinges on the specimen perpendicularly to the symmetry axis. The equatorial component of the scattering vector is denoted as s where s is related to the scattering angle on the equator 2θ and the X-ray wavelength λ by the equation

$$s = \frac{2}{\lambda}\sin\theta \tag{11}$$

The total scattering intensity, along a line parallel to the meridian, at an equatorial position s is denoted as $I(s)$. Then, the parameter v can be determined as

$$v = \frac{2\pi m^2 c^4 D}{e^4\lambda\rho^2\tau t A I_o}\int_0^\infty I(s)s\,\mathrm{d}s \tag{12}$$

where c is the velocity of light, e the elementary electric charge, m the electron mass, AI_o the incident X-ray beam flux, D the specimen-to-detector distance, ρ the electron density difference between microvoids and surrounding solid, τ the X-ray transmittance of the specimen, and t the specimen thickness. The incident X-ray beam flux can be determined, for example, by comparing the theoretical and the measured scattering intensities of air.[25] The parameters R_3 and S_3 can be determined form the slope and the intercept of the line approximating ln $I(s)$ vs s^2 plots in a smaller angle range according to the following equation:

$$\ln I(s) = -2\pi^2 R_3^{\,2}s^2 + \ln\left[2\pi S_3\int_0^\infty I(s)s\,\mathrm{d}s\right] \quad \text{(smaller angle range)} \tag{13}$$

The parameter l_2 can be determined as

$$l_2 = \frac{1}{\pi}\frac{\int_0^\infty I(s)\,\mathrm{d}s}{\int_0^\infty I(s)s\,\mathrm{d}s} \tag{14}$$

The parameter l_3 can be determined form the slope of the line approximating $I(s)^{-2/3}$ vs s^2 plots in the larger angle range according to the following equation:

$$I(s)^{-2/3} = \left[\frac{1}{2\pi l_3}\int_0^\infty I(s)s\,\mathrm{d}s\right]^{-2/3}\left[s^2 + \frac{1}{4\pi^2 l_3^{\,2}}\right] \quad \text{(larger angle range)} \tag{15}$$

The integration of the intensity in the above equations at very small and large angles can be carried out by extrapolating the intensity distribution according to eqs 13 and 15.

In addition to the transverse sizes of the microvoids shown above, the longitudinal size of the microvoids can be determined from the equatorial streak as follows. If the microvoids are of columnar shape, uniform in shape and size, and oriented with the height directions of the columns in parallel to the fiber axis, the height of the columns, i. e. the longitudinal length of the microvoids, L can be determined from the intensity distribution, in parallel to the meridian, of the equatorial streak according to the equation

$$L = \sqrt{\frac{4\ln 2}{\pi}}\frac{1}{\Delta s} \tag{16}$$

where Δs is the fwhm in s of the intensity distribution and s is the meridional component of the scattering vector defined similarly to eq 11.

The microvoids were analyzed using different samples from those used for characterizing the fiber structure at small fiber strains since the exposure time of the CCD camera appropriate

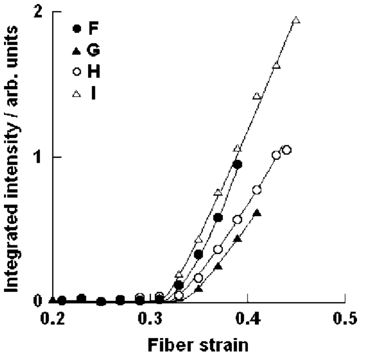

Figure 8. Integrated intensity of equatorial streak versus fiber strain for samples F−I.

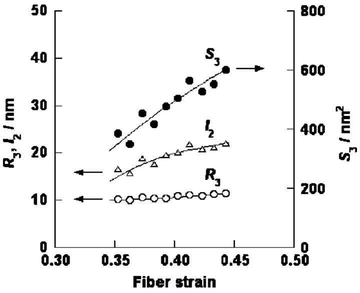

Figure 9. Size parameters of transverse cross sections of microvoids S_3, R_3, and l_2 versus fiber strain for sample H.

for detecting the equatorial streak was much shorter than that for detecting the layer-line scattering. Determination of v using eq 12 requires the density, X-ray transmittance and thickness of the specimen in addition to the incident X-ray beam flux. Since these values for the deformed fibers were not measured in the present experiments, the integrated intensity, i.e., the values of the integration in eq 12, are evaluated as a rough estimate of the relative microvoid volume fraction.

The integrated intensities of the equotorial streaks for several samples (samples F−I) are plotted against fiber strains in Figure 8. This figure shows that the microvoids are formed at the fiber strain of about 0.3, and their volume fraction continuously increases thereafter up to fiber fracture.

The size parameters S_3, R_3, and l_2 for sample H are plotted against the fiber strain in Figure 9. The size parameters increase with the fiber strain but the variation is mach slower than that of the microvoid volume fraction. The size parameters are not zero when the equatorial streak begins to appear. It seems that the microvoids have certain sizes even when they are created and the increase of the microvoid volume fraction is brought about mainly by the increase in the number of the microvoids with similar sizes. It is, therefore, possible to assume that the size distribution of the microvoid cross sections at a given fiber strain is also narrow. With the assumption that the microvoid cross sections are of uniform elliptic shape, the aspect ratio μ and the semiminor axis r were determined from the values of R_3 and S_3 using eqs 7 and 8. The major axis 2 μr and the minor axis $2r$ of the transverse cross sections of the microvoids and the longitudinal length of the microvoids L determined according to eq 16 are shown against the fiber strain in Figure 10. In order to check the validity of the assumption that the microvoid cross sections are of uniform elliptic shape, the values of l_2 were calculated from μ and r according to eq 9 and compared with those measured in Figure 11. Since the calculated values of l_2 agree well with those measured, the assumption is not unreasonable. It should be mentioned, however, that the coincidence of the calculated values of l_2 with the measured values does not mean that there is no other possible combination of the shape and the size of the microvoid cross sections that is consistent with the measured values of S_3, R_3, and l_2.

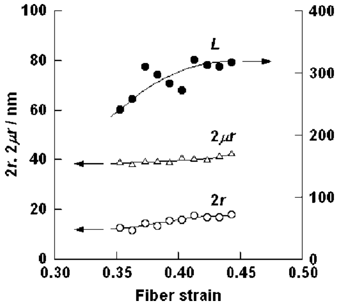

Figure 10. Lengths of major axis 2 μr and minor axis $2r$ of transverse cross sections of microvoids and longitudinal length of microvoids L versus fiber strain for sample H.

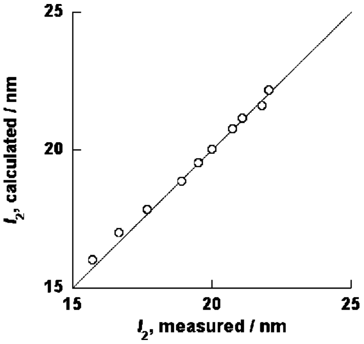

Figure 11. Values of l_2 calculated from eq 9 versus measured values of l_2 for sample H.

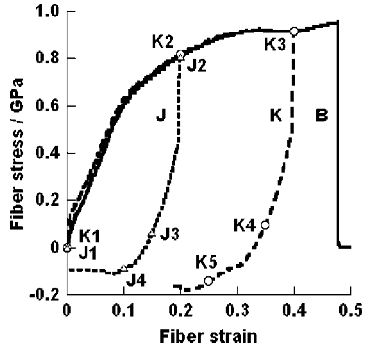

Figure 12. S−S curves for PET fibers with which movement of chucks was reversed before fiber fracture (samples J and K) and not reversed (sample B).

Figure 10 indicates that the microvoids are of ribbonlike shape with a length of about 290 nm, a width of about 40 nm, and a thickness of about 15 nm. The microvoids are much larger than the bundle of long-period structures.

Reversibility of Structure Changes. For samples J and K, the movement of the chucks of the tensile testing machine was reversed before fiber fracture in order to investigate the reversibility of structure changes. The movement of the chucks was reversed for samples J and K at the fiber strains of 0.2 and 0.4, respectively, as can be seen in the S−S curves of Figure 12. The negative stress at the end of unloading is due to the frictional force of the tensile testing machine. The frictional force during loading was canceled by adjusting the load amplifier but that during unloading could not be canceled since the directions

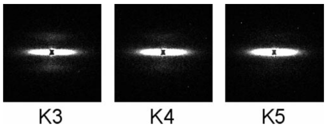

Figure 13. SAXS patterns of sample K at points K3−K5 on the S−S curve shown in Figure 12. Fiber axis is in the top and bottom direction.

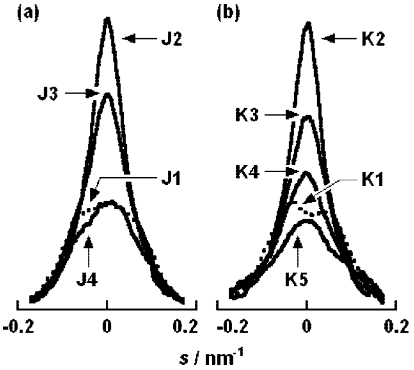

Figure 14. Intensity distributions, along layer line, of layer-line scattering for samples J and K at points J1−J4 (a) and K1−K5 (b) on the S−S curves shown in Figure 12. Abscissa *s* is equatorial component of scattering vector.

of the frictional forces during loading and unloading were opposite.

The SAXS patterns of sample K at points K3−K5 on the S−S curve of Figure 12 are compared in Figure 13. The equatorial streak produced during loading (K3) remains after the fiber stress is removed (K4 and K5). Once the microvoids are formed, they do not disappear by the removal of the fiber stress. The intensity distribution, along the layer line, of the layer-line scattering of samples J and K at points J1−J4 and K1−K5 are compared in Figure 14. The layer-line scattering of sample-J before tensile deformation (J1) did not show the four-spot nature probably because of the fluctuation of the fiber structure along a filament. With this sample, the intensity maximum increased accompanied by the decrease in fwhm during loading (J2). During unloading, the intensity decreased (J3) and nearly the initial intensity distribution was recovered when the fiber stress was removed (J4). With sample K, the change of the intensity distribution up to the fiber strain of 0.2 (K2) was similar to that of sample J. When the fiber strain increased from 0.2 (K2) to 0.4 (K3), the intensity maximum decreased accompanied by the increase in fwhm. This suggests that the longitudinal disorder of the arrangements of the transversely neighboring crystalline regions ω_{13}, which has once decreased at small fiber strains, increased again at large fiber strains. After removal of the fiber stress (K5), although the initial four-spot nature of the intensity distribution (K1) was not recovered, the intensity level was close to the initial one. The changes of the scattering patterns during unloading (K3−K5) indicate that there is an elastically recoverable component in the deformation of the bundle of long-period structures.

Discussion

Cavitation of polymer glasses which arises under tensile deformation is known as crazing. Crazes are the regions bounded by two flat surfaces perpendicular to the loading direction. In the crazes, thin fibrils parallel to the loading direction bridge the two surfaces and interconnecting voids surround them. Unlike cracks, the crazes have load bearing capability endowed by the fibrils and the energy dissipation during stable growth of crazes contributes to the fracture toughness. The crazes eventually turn into true cracks at the breakdown of fibrils and propagate through the polymer glasses leading to the macroscopic fracture.

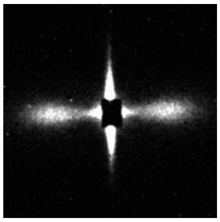

Figure 15. SAXS pattern of unoriented amorphous PET film under tensile deformation at room temperature. The loading axis is in the top and bottom direction.

The nucleation and the growth of crazes proceed in the following manner:[32] The stress at any point of the material can be represented as the sum of the hydrostatic stress and the deviatoric stress. Voids are formed where the local hydrostatic stress reaches a large negative pressure near the defects such as surface grooves, second phase particles, dust particles, and the regions with different molecular orientation. Subsequently, the voids interconnect while the remaining ligaments between the voids are hardened with increased molecular orientation, forming the nuclei of crazes. With further macroscopic deformation, crazes grow stably by the advance of the craze tip perpendicular to the loading direction (craze tip advance) and the increase in the separation between the two surfaces (craze thickening) until fibrils break down. During the craze thickening, the fibril length increases by drawing new polymer from the craze/intact polymer interfaces (strain softened polymer layer or active zone) into fibrils by maintaining constant extension ratio of the molecules in fibrils (surface drawing mechanism). The molecular entanglements have important influences on the evolution of crazes. A certain amount of entanglements is necessary for stabilizing the crazes as is known from the existence of a critical molecular weight below which stable crazes do not form and polymer glasses become very brittle. With increasing entanglement density, on the other hand, the stress to form crazes gets larger than the stress to cause shear deformation, and the polymer glasses deform in shear without forming crazes. The prior molecular orientation also strongly influences the evolution of crazes.

The PET molecules used in this study had the capability to form crazes when they are processed into unoriented amorphous films. Figure 15 shows the SAXS pattern of this film which was obtained by introducing a surface notch, applying tensile deformation perpendicularly to the notch surface, and irradiating the ligament with the synchrotron X-ray beam perpendicular to the film surface. The cross-shaped pattern shown in this figure originates from the crazes and consists of the streak parallel to the loading direction due to the total reflection at craze/intact polymer interfaces and the streak perpendicular to the loading direction caused by the fibril/void structure in the crazes. The intensity distribution, perpendicular to the loading direction, of the later streak has intensity maximum corresponding to the period of 23 nm indicating that the fibrils are arranged in the crazes with certain degree of regularity. From the fwhm of the intensity distribution, parallel to the loading direction, of this streak, the length of the fibrils are roughly estimated to be 80 nm.

Referring to the craze formation mechanism described above, the following mechanism can be proposed for the formation of microvoids in the PET fiber having a larger fiber strain at fracture (sample B): The strain of the long-period structures which initially coincides with the fiber strain gets smaller than the fiber strain beyond the fiber strain of about 0.1. This implies that the strain of the regions which mechanically link longitudinally neighboring long-period structures (linking region) is larger than the strain of the long-period structures. The linking regions do not have the regular periodic arrangements of the crystalline and the amorphous regions and some of them may be rich in amorphous polymer chains. These regions have smaller rigidity than the long-period structures. Since the tensile stresses in the linking regions and the long-period structures are the same if they are linked in series, the linking regions store a larger strain energy than the long-period structures do. Microvoids are formed in these regions due to the negative pressure there. The strain energy is dissipated through the deformation of polymer chains into the ligaments with a higher molecular orientation such as fibrils and microvoid walls. The existence of the remaining ligaments is suggested by the recoverability of the strain of the long-period structures upon unloading. The formation of microvoids in the amorphous regions of the long-period structures is suppressed because of the constraint of the deformation of the molecules imposed by the longitudinally neighboring crystalline regions. This inference is consistent with the sizes of microvoids which are extremely larger than those of the amorphous regions in the long-period structures. The advance of the defective structure containing microvoids transversely to the loading direction is prevented by the existence of transversely neighboring long-period structures. Thus, unlike crazes, the isolated microvoids are formed in the fiber without positional correlation between them. The length of the microvoids are also limited by the initial length of the linking region.

In the case of the PET fiber having a smaller fiber strain at fracture (sample A), the strain of the long-period structures beyond the fiber strain of about 0.1 is much smaller. This implies that the rigidity of the linking regions are much smaller. These regions fracture without forming the ligaments with a higher molecular orientation necessary for the stress transfer during further loading, resulting in the fiber fracture.

As shown above, the formation and the sizes of the microvoids in the PET fibers used in this study is determined by the strength and the sizes of the linking regions. The formation of microvoids contributes to the fracture toughness of fibers similarly to the crazing in films. Murthy et al.[19] have investigated the structure−property relationships of the four generations of PET fibers having fiber strains at fracture from 10 to 14% and concluded that the fibers in which better stress transfer to the crystalline regions as a result of strong linkages to the amorphous regions had a higher modulus and a lower strain at fracture. The influence of the effective stress transfer to the long-period structures on the fiber strain at fracture differs between their results and ours probably because of the structure of fibers, especially the structure of the linking regions.

Conclusions

SAXS measurements were conducted during tensile deformation of a PET fiber at room temperature, and the results were analyzed utilizing the methods proposed by the present authors. The marked change of the scattering patterns from the layer-line scattering with a four-spot nature to the layer-line scattering concentrated on the meridian at small fiber strains was attributed to the slight decrease in the longitudinal disorder of the arrangements of the transversely neighboring crystalline regions in a bundle of long-period structures. The strain of the long-period structure increased in accordance with the external fiber strain at small fiber strains while it deviated from the fiber strain at large fiber strains. Microvoids much larger than the long-period structures were formed at a large fiber strain in the regions which linked the long-period structures and the number of the microvoids continued to increase with increasing fiber strain up to fiber fracture. Concomitantly with the formation of microvoids, the ligaments which continued to sustain the fiber load were formed in the linking regions. The formation of microvoids, which depended on the strength of the linking regions, contributed to the fracture toughness of the fiber.

Acknowledgment. This work was supported by the High-Strength Fiber Project, Technology for Precisely Controlled Polymers, Nanotechnology Program for Materials Development promoted by New Energy and Industrial Technology Development Organization, Japan. The measurements of SAXS were performed at BL15A of Photon Factory, High Energy Accelerator Research Organization, Japan under the approval of the Photon Factory Program Advisory Committee (Proposal Nos. 2004G311 and 2006G091).

References and Notes

(1) Kikutani, T. *J. Appl. Polym. Sci.* **2002**, *83*, 559–571.
(2) Kikutani, T. *Int. Symp. Nanostruct. Polym. Mater. Prepr.* **2003**, 84–87.
(3) Yeh, G. S. Y.; Geil, P. H. *J. Macromol. Sci. B* **1967**, *1*, 251–277.
(4) Fischer, E. W.; Fakirov, S. *J. Mater. Sci.* **1976**, *11*, 1041–1065.
(5) Welsh, G. E.; Blundell, D. J.; Windle, A. H. *Macromolecules* **1998**, *31*, 7562–7565.
(6) Asano, T.; Calleja, F. J. B.; Flores, A.; Tanigaki, M.; Mina, M. F.; Sawatari, C.; Itagaki, H.; Takahashi, H.; Hatta, I. *Polymer* **1999**, *40*, 6475–6484.
(7) Mahendrasingam, A.; Blundell, D. J.; Martin, C.; Fuller, W.; MacKerron, D. H.; Harvie, J. L.; Oldman, R. J.; Riekel, C. *Polymer* **2000**, *41*, 7803–7814.
(8) Welsh, G. E.; Blundell, D. J.; Windle, A. H. *J. Mater. Sci.* **2000**, *35*, 5225–5240.
(9) Gorlier, E.; Haudin, J. M.; Billon, N. *Polymer* **2001**, *42*, 9541–9549.
(10) Ran, S.; Wang, Z.; Burger, C.; Chu, B.; Hisao, B. S. *Macromolecules* **2002**, *35*, 10102–10107.
(11) Kawakami, D.; Hsiao, B. S.; Ran, S.; Burger, C.; Fu, B.; Sics, I.; Chu, B.; Kikutani, T. *Polymer* **2004**, *45*, 905–918.
(12) Stribeck, N.; Fakirov, S.; Apostolov, A. A.; Denchev, Z.; Gehrke, R. *Macromol. Chem. Phys.* **2003**, *204*, 1000–1013.
(13) Stockfleth, J.; Salamon, L.; Hinrichsen, G. *Colloid Polym. Sci.* **1993**, *271*, 423–435.
(14) Kobayashi, H.; Shioya, M.; Tanaka, T.; Irisawa, T. *Compos. Sci. Technol.* **2007**, *67*, 3209–3218.
(15) Kobayashi, H.; Shioya, M.; Tanaka, T.; Irisawa, T.; Sakurai, S.; Yamamoto, K. *J. Appl. Polym. Sci.* **2007**, *106*, 152–160.
(16) Zheng, Z.; Nojima, S.; Yamane, T.; Ashida, T. *Macromolecules* **1989**, *22*, 4362–4367.
(17) Murthy, N. S.; Grubb, D. T. *J. Polym. Sci., Part B: Polym. Phys.* **2006**, *44*, 1277–1286.
(18) Murthy, N. S.; Grubb, D. T. *J. Polym. Sci., Part B: Polym. Phys.* **2002**, *40*, 691–705.
(19) Murthy, N. S.; Grubb, D. T. *J. Polym. Sci., Part B: Polym. Phys.* **2003**, *41*, 1538–1553.
(20) Song, H. H.; Argon, A. S.; Cohen, R. E. *Macromolecules* **1990**, *23*, 870–876.
(21) Murthy, N. S.; Grubb, D. T.; Zero, K. *Macromolecules* **2000**, *33*, 1012–1021.
(22) Shioya, M.; Kawazoe, T.; Kojima, J.; Sakurai, S.; Yamamoto, K.; Kikutani, T. *Polymer* **2006**, *47*, 3616–3628.
(23) Wu, J.; Schultz, J. M.; Yeh, F.; Hsiao, B. S.; Chu, B. *Macromolecules* **2000**, *33*, 1765–1777.
(24) Grubb, D. T.; Prasad, K.; Adams, W. *Polymer* **1991**, *32*, 1167–1172.
(25) Shioya, M.; Takaku, A. *J. Appl. Phys.* **1985**, *58*, 4074–4082.
(26) Takaku, A.; Shioya, M. *J. Mater. Sci.* **1986**, *21*, 4443–4450.
(27) Fakirov, S.; Fischer, E. W.; Schmidt, G. F. *Makromol. Chem.* **1975**, *176*, 2459–2465.
(28) Goschel, U.; Deutscher, K.; Abetz, V. *Polymer* **1996**, *37*, 1–6.
(29) Daubeny, R. D.; Bunn, C. W.; Brown, C. J. *Proc. R. Soc. London Ser. A* **1954**, *226*, 531–542.
(30) Heuvel, H. M.; Huisman, R. *J. Appl. Polym. Sci.* **1978**, *22*, 2229–2243.
(31) Samon, J. M.; Schultz, J. M.; Hsiao, B. S. *Polymer* **2000**, *41*, 2169–2182.
(32) Kramer,E. J. *Crazing in Polymers*; Springer-Verlag: Berlin, 1983; pp 1−56.

MA7027616